

Mesoscopic Theory of Wavefront Shaping to Focus Waves inside Disordered Media

Bart A. van Tiggelen

*Université Grenoble Alpes, Centre National de la Recherche Scientifique (CNRS),
Laboratoire de Physique et de Modélisation des Milieux Condensés (LPMMC), 38000 Grenoble, France**

Ad Lagendijk

*Complex Photonic Systems (COPS), MESA+ Institute for Nanotechnology,
University of Twente, P.O. Box 217, 7500 AE Enschede, The Netherlands*

Willem L. Vos

*Complex Photonic Systems (COPS), MESA+ Institute for Nanotechnology,
University of Twente, P.O. Box 217, 7500 AE Enschede, The Netherlands and
Université Grenoble Alpes, Centre National de la Recherche Scientifique (CNRS),
Laboratoire de Physique et Modélisation des Milieux Condensés (LPMMC), 38000 Grenoble, France*

(Dated: 14 october 2024)

We describe the theory of focusing waves to a predefined spatial point inside a disordered three-dimensional medium by the external shaping of N different field sources outside the medium, also known as wavefront shaping. We derive the energy density of the wave field both near the focal point and anywhere else inside the medium, averaged over realizations *after* focusing. To this end, we conceive of a point source at the focal point that emits waves to a detector array that - by time reversal - emits the desired shaped fields. It appears that the energy density is formally equal to intensity speckle described by the so-called C_1 , C_2 , C_3 and even C_0 correlations in mesoscopic transport theory, yet the density also obeys a diffusion equation. The C_1 correlations describes the focusing in the random medium very well, but do not generate a new source of energy that is conceived at the focal point. A source emerges only when the C_2 speckle is incorporated. The role of C_0 speckle, describing fluctuations in the local density of optical states (LDOS) is also investigated, but hardly plays a role in the focusing. Finally, we use the concept of an energy source inside the medium to model the well-known optimized transmission by a slab using wavefront shaping.

I. INTRODUCTION

Waves can be focused to predefined points by the manipulation of incident wave fronts [1]. This new method is now well known in optics as "wavefront shaping" (WFS) [2]. In a disordered medium, WFS is efficient because multiple scattering is characterized by short range correlations that can suppress statistical fluctuations. In this procedure, with many potential applications, one manipulates the phases and amplitudes of spatial or spectral elements of an incident wave packet to optimize either the focusing to a predefined point, the total transmission, or even the delay time [3]. Recent work concentrated not just on the focusing but also on the energy density of the waves inside the medium after wave front shaping. It was found that after optimizing transmission, the density profile inside the medium is dominated by the first eigenmode of the diffusion equation [4], as confirmed by Davy *et al.* [5] and Koirala *et al.* [6]. This surprising feature is remarkable yet no simple explanation has been given to date.

In this work we analyze the WFS to focus an incident wave packet to a given point deep in a disordered slab or half-space. In Figure 1 we show the set-up for a disordered half-space. We use a mesoscopic theory with a

statistical approach to deal with wave fluctuations. This approach does not reveal information on individual realizations, such as the specific realization that optimizes some observable. Nevertheless, given a specific realization of the disorder, the wave front to be emitted by an array of sources designed to optimally focus to a point S inside the random medium can be obtained by first sending a wave packet from a virtual source at S , and time-reverse the received signal at the array. Previous work has established that the focusing is stabilized by short-range correlations and close to the statistical average [7]. The important role of non-Gaussian mesoscopic fluctuations has also been addressed [8].

We will assume a monochromatic wave packet and an array with angular opening Ω_A . This array sends plane waves with propagation directions inside the solid angle Ω_A when the phases emitted by the different elements $\{\mathbf{x}_i\}$ vary linearly. When they are manipulated otherwise, many complicated wave fronts can be achieved. Here we want to employ WFS to focus to a point S in the medium. The time-reversal method implicitly generates an ideal candidate, not necessarily unique. In addition, scattering from disorder generates an background energy density of the wave field that varies with the position of point R in Figure 1. Intuitively, we may expect the focal point S to become a secondary source of energy for diffuse waves in the random medium and contribute to this background energy. We will analyze different correlations of type C_0 (fluctuations in density of states),

* Bart.Van-Tiggelen@lpmmc.cnrs.fr

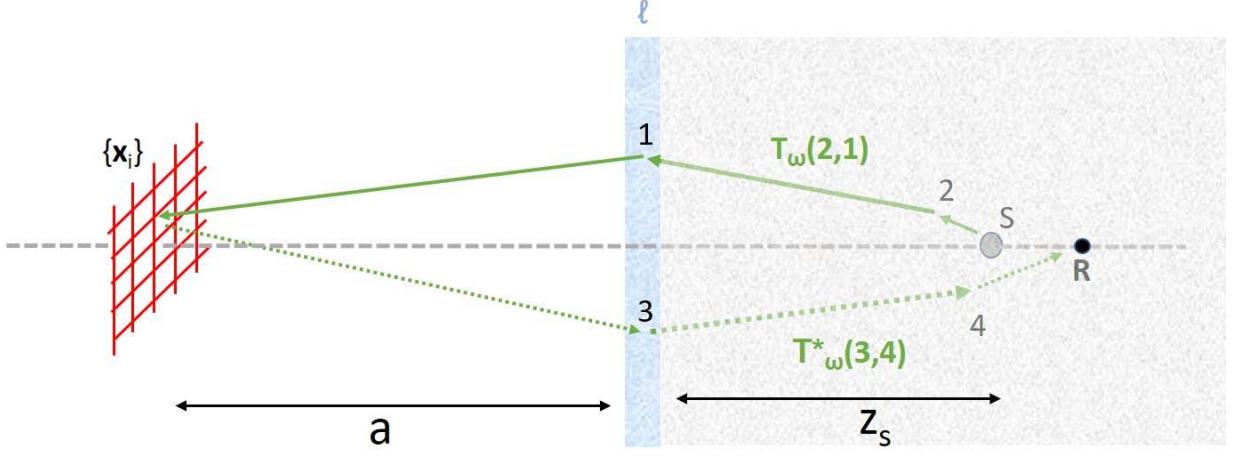


Figure 1. Schematic of wavefront shaping to focus waves to a point S inside a disordered 3D half-space on the right. The medium has a skin layer with a depth equal to about one mean free path ℓ . A wave packet from a virtual point source at S is sent towards the detector array with N detectors at positions $\{\mathbf{x}_i\}$ in the "far field" of the medium, meaning here that $a \gg z_S$. The optimal shaping is established by time-reversal of the entire wave packet. It necessarily refocuses on a diffraction-limited spot $R \approx S$ with a background energy that is calculated in this work for all positions R . The path of the wave from source to array is separated into 3 parts: a) release of energy by a virtual source at focus S to a nearby scatterer 2, b) radiative transport towards a position 1 in the skin layer with T -matrix $T_\omega(2,1)$, and c) ballistic propagation from skin layer towards array. The same is done for the time-reversed signal, here equal to the complex conjugate and shown as a dashed line.

C_1 (Gaussian speckle of intensity) and C_2 (correlations in total transmission) known in mesoscopic wave physics, and show that C_2 makes a dominant contribution to the energy density of the waves away from focal spot, and also generates this expected source.

Because diffusion is taken to be isotropic, the typical diffuse halo created by a virtual source at depth z_S has size z_S . We will also assume that the distance a of the array satisfies $a \gg z_S$. In that case, waves arriving at points 1 and 3 in Figure 1 still have approximate normal incidence. The average propagation from array to skin layer is described by the Green function

$$G(i, 1) = -\frac{1}{4\pi|\mathbf{r}_i - \mathbf{r}_1|} e^{ik|\mathbf{r}_i - \mathbf{r}_1|} e^{-z_1/2\ell \cos \theta} \approx -\frac{1}{4\pi a} e^{ika} e^{-ik\rho_1 \cdot \mathbf{x}_i/a} e^{-z_1/2\ell} \quad (1)$$

Near points R and S deep in the medium we adopt the bulk expression for average wave propagation,

$$G(S, 2) = -\frac{1}{4\pi|\mathbf{r}_S - \mathbf{r}_2|} e^{i(k+i/2\ell)|\mathbf{r}_S - \mathbf{r}_2|} \quad (2)$$

which restricts the position of point 2 within a mean free path ℓ from S .

II. TIME-REVERSAL TO OPTIMIZE WAVE FRONT

Let us briefly recall the process of time-reversal, adapted to the present simplified context. For scalar

waves, time-reversal reduces to complex conjugation. When the virtual source at S starts releasing its energy at $t = 0$, the field is registered outside the medium on the array between times $0 < t < T$, sent back time-reversed immediately and measured at point R at time $\tau > T$. We assume that the signal has a spectral bandwidth B small enough to be considered quasi-monochromatic but that $T \gg 2\pi/B$. The field sent back to the medium and arriving at R is then given by [10, 11]

$$\Phi(R, \tau + 2T) = \int_{-\infty}^{\infty} \frac{d\omega}{2\pi} e^{-i\omega\tau} s(\omega) \times G_{S \rightarrow \{\mathbf{x}_i\}}(\omega + i0) G_{\{\mathbf{x}_i\} \rightarrow R}^*(\omega + i0) \quad (3)$$

From previous work we know that this signal typically contains an arrival at $\tau < 0$ and - by reciprocity - one at $\tau > 0$ associated with waves traveling from S to R and vice-versa. In the frequency domain, we can split this propagation up into different parts as shown in Figure 1,

$$\Phi(R, \omega) = D \sum_{i=1}^N \int_{1,2,3,4} G(S, 2) T(2, 1) G(1, i) \times G^*(i, 3) T^*(3, 4) G^*(4, R) \quad (4)$$

with all factors taken at equal frequency, therefore the label is omitted. We have summarized the "virtual" source intensity of S and any possible loss or gain factor in time-reversal by a complex number D . Hereafter we shall put $F = D/(4\pi a)^2$ as the typical amplitude of the incident

wave front arriving at the boundary (with same unit as the field itself). The quality of focusing is determined by 1) the size of the focal spot around S , and 2) the ratio of peak value in energy at S and surrounding ‘‘average background’’. As mentioned earlier, we expect this background to contain a component associated with a real source at S . In time-reversal experiments, a large enough bandwidth (larger than the Thouless frequency proportional to D/z_s^2 that determines uncorrelated frequencies) guarantees self-averaging and stability of the process. In this work this is provided by the opening of the array.

A. C_1 correlations

The ensemble-average of the energy density $\langle |\Phi(R)|^2 \rangle$ contains *four* T-matrices. In the well-known C_1 approximation we have Gaussian decoupling of complex conjugates [12],

$$\begin{aligned} \langle T(2,1)T^*(3,4)T^*(2',1')T(3',4') \rangle = \\ \langle T(2,1)T^*(3,4) \rangle \langle T^*(2',1')T(3',4') \rangle \\ + \langle T(2,1)T^*(2',1') \rangle \langle T^*(3,4)T(3',4') \rangle \end{aligned} \quad (5)$$

where the accents refer to the positions in the path followed by the time-reversed path. The first term is just equal to the average field squared and peaks at $R \approx S$. This follows from the equality

$$\int_2 G(S,2)G^*(2,R) = \frac{\ell}{4\pi} \frac{\text{Im } G(S,R)}{\text{Im } G(0)} \equiv \frac{\ell}{4\pi} P(S,R) \quad (6)$$

which describes a diffraction-limited peak near S oscillating at the scale of the wavelength and decaying exponentially with the mean free path ℓ . In the diffusion approximation we have

$$\langle T(2,1)T^*(3,4) \rangle = L(1,2) [\delta_{13}\delta_{24} + \delta_{12}\delta_{34}] \quad (7)$$

with the propagator L obeying the stationary diffusion equation

$$-\frac{1}{3}\ell^* \nabla_1^2 L(1,2) = \frac{4\pi}{\ell^2} \delta_{12} \quad (8)$$

where ℓ^* is the transport mean free path. To simplify, we will assume $\ell^* = \ell$ in the rest of this work. The two terms in Eq. (7) are imposed by reciprocity but the second ‘‘Coherent Backscattering’’ term only contributes when point 1 is close to point 2, and is here excluded because 1 is located in the skin layer and 2 is close to S deep in the bulk. With the approximations explained above we obtain for the peak energy density P_1 (averaging brackets are dropped for simplicity),

$$\begin{aligned} P_1(R,S) = |F|^2 N^2 \left(\frac{\ell}{4\pi} \right)^2 P(S,R)^2 \\ \times \left| \int_0^\infty dz_1 e^{-z_1/\ell} L(z_S, z_1, \mathbf{q} = 0) \right|^2 \end{aligned}$$

with N the number of elements in the array all contributing equally and coherently, and \mathbf{q} the transverse Fourier component. Here, $\mathbf{q} = 0$ appears because the effective area $\sim z_s^2$ illuminated by the virtual source is much smaller than the area $\sim a^2$ available. If we impose the usual radiative boundary condition $L(-z_0, z) = 0$ for all z , with $z_0 \approx \frac{2}{3}\ell$, it follows that $L(z, z', \mathbf{q} = 0) = (12\pi/\ell^3)[z_0 + \min(z, z')]$. To avoid messy formulas especially later we will approximate the integrals $\int dz \exp(-z/\ell)f(z) \approx \ell f(0)$. Then, for $z > 0$,

$$P_1(S,R) = 9|F|^2 N^2 P(S,R)^2 \left(\frac{z_0}{\ell} \right)^2 \quad (9)$$

According to this expression, not valid for S near the boundary, the focused energy spot is independent of the depth of S . We emphasize that the spot is not due to a local energy source (see Appendix B). In this steady state picture, the focus is due to constructive interference between incoming and outgoing waves at S that causes the energy to accumulate locally, much like what happens in the focal spot after time-reversal [13].

The second term in Eq. (5) is usually associated with short-range speckle correlations, but here generates a ‘‘diffuse’’ background energy B_1 , *i.e.*, that depends on R but without a distinguished peak near S . This background suffers from dephasing between the phase factors $\exp(i\boldsymbol{\rho}_i \cdot \mathbf{x}_i/a)$ in Eq. (1),

$$B_1(z, \boldsymbol{\rho}) = |F|^2 \frac{\ell^4}{(4\pi)^2} \sum_{ij} L(0, z_S, \mathbf{q}_{ij}) L(0, z, \mathbf{q}_{ij}) e^{i\mathbf{q}_{ij} \cdot \boldsymbol{\rho}} \quad (10)$$

with the transverse wave vector $\mathbf{q}_{ij} = k(\mathbf{x}_i - \mathbf{x}_j)/a$ governing interference between different array elements. For finite \mathbf{q} , the diffusion propagator takes the form,

$$L(z, z', \mathbf{q}) = \frac{12\pi}{\ell^3} \frac{e^{-q|z-z'|} - e^{-q(z+z'+2z_0)}}{2q}$$

If the typical distance between array elements obeys $\Delta x < (\lambda/2\pi)a/z_s$, clearly true if $a \gg z_s$, the sum over j reaches the continuum limit so that we can replace by an integral, that in addition is independent on i since for $z_S \gg \ell$ the propagator $L(z_S, 0, q)$ decays rapidly with q . We introduce $N(\Delta x)^2/a^2 = \Omega_A$ as the total angular opening of the array. We assume $\Omega_A < 1$ so that approximate normal incidence remains valid for all array elements without the need for Ω_A to be very small. For $z > 0$ the expression for B_1 reduces to

$$\begin{aligned} B_1(z, \boldsymbol{\rho}) &= \frac{|F|^2 N^2 \ell^4}{(4\pi)^2 k^2 \Omega_A} \int d^2 \mathbf{q} L(0, z_S, \mathbf{q}) L(0, z, \mathbf{q}) e^{i\mathbf{q} \cdot \boldsymbol{\rho}} \\ &= 9|F|^2 N^2 \frac{z_0^2}{\ell^2} \frac{2\pi z_0^2}{k^2 \Omega_A} \frac{z + z_S + 2z_0}{[(z + z_S + 2z_0)^2 + \rho^2]^{3/2}} \end{aligned} \quad (11)$$

For S near the boundary this is proportional to the familiar emission of a diffuse point source created by a focus

from outside [?]. For S deep in the medium the energy density is roughly constant as long as $z, \rho < z_S$. The diffuse transverse halo has a typical surface that grows with depth according

$$\langle \rho^2(z, z_S) \rangle_1 \equiv \frac{\int d^2 \boldsymbol{\rho} B_1(z, \boldsymbol{\rho})}{B_1(z, \boldsymbol{\rho} = 0)} = 2\pi(z + z_S + 2z_0)^2 \quad (12)$$

and is small compared to πa^2 at the surface ($z = 0$) when $z_S \ll a$, justifying an earlier assumption. We can compare the background energy density near $S = (z_S, \boldsymbol{\rho} = 0)$ to the peak value given by Eq. (9),

$$\frac{B_1(R = S)}{P_1(R = S)} \approx \frac{2\pi/[2k(z_S + z_0)]^2}{\Omega_A} \quad (13)$$

This expression shows that in the C_1 approximation the typical angular correlation for WFS to a point S deep inside the half-space is $\delta\Omega \sim 2\pi/(2kz_S)^2$. The conclusion is that the finite angular coverage - even small - suppresses the C_1 background and makes the focus prominent and stable against statistical fluctuation in the medium [7].

In Appendix A we show that the background energy density B_1 , despite being produced here by a preceding time-reversal procedure, obeys the usual diffusion equation known for diffuse energy produced by normal incident radiation, in particular with the same diffusion constant D . The diffusion equation is also characterized by a source of energy, proportional to $-\nabla^2 B_1$. From Eq. (11) we infer that this source is proportional to $L(0, z_S, \boldsymbol{\rho})\delta(z) \sim \delta(z) \times z_S/(z_S^2 + \rho^2)^{3/2}$, *i.e.*, only at the surface boundary and with a finite transverse width equal to z_S . Because no other source exists in the medium and also no flux is transmitted, the energy flux F_1 across any transverse surface given by,

$$F_1(z > 0) = \int d^2 \boldsymbol{\rho} J(z, \boldsymbol{\rho}) = -D\partial_z \int d^2 \boldsymbol{\rho} B_1(z, \boldsymbol{\rho}) = 0, \quad (14)$$

vanishes. Nevertheless, for any $z > 0$ and for fixed $\boldsymbol{\rho}$, the current density itself does not vanish. Since the incoming flux vanishes due to the radiative boundary condition $B_1(-z_0) = 0$, the totally reflected (average) flux is given by

$$\begin{aligned} F_1(z < 0) &= -D \int d^2 \boldsymbol{\rho} \partial_z B_1(z < 0, \boldsymbol{\rho}) \\ &= -\frac{9|F|^2 N^2 (2\pi)^2 z_0^2}{(k\ell)^2 \Omega_A} \times \frac{c_0}{2} \end{aligned} \quad (15)$$

with $z_0 = 2\ell/3$ and $D = c_0\ell/3$. We need this outgoing flux later when we include C_2 to normalize the reflection coefficient.

Finally, one may wonder how nearby scatterers affect the focusing profile. They are not taken into account by the present approach. In Appendix C we discuss these so-called C_0 correlations. The conclusion is that they perturb the peak profile and have relative weight $1/k\ell$ compared to the peak value (9). They do not contribute to background.

III. C_2 CORRELATION AND SOURCE

In this section, we investigate the importance of C_2 correlations for the focusing of energy at point S and its energy density around. The two diagrams are shown in Figure 2. The figure on the left is expected to contribute to the background because it is proportional to $\delta_{13}\delta_{1'3'}\delta_{22'}\delta_{44'}$. This links both endpoints 4 and 4' to the point of observation R and does not decorrelate when R changes (recall Figure 1). In addition, since 1, 3 and 1', 3' are linked the diagram is also insensitive to phase differences between received and emitted waves by the array, as was the case for the peak energy in Eq. (9). The figure on the right on the other hand is proportional to $\delta_{24}\delta_{2'4'}$ and only survives when R and S are separated by at most one mean free path and thus contributes to focalization. The decorrelation between different array elements makes it a factor $\Omega_A(kz_S)^2$ smaller. The diagram on the left is expressed mathematically as [12].

$$\begin{aligned} \langle T(2, 1)T^*(3, 4)T^*(2', 1')T(3', 4') \rangle_{C_2} = \\ N_H \int d^3 \mathbf{H} \left[\nabla_a \cdot \nabla_b + \nabla_c \cdot \nabla_d - \frac{1}{2} \sum_i \nabla_i^2 \right]_{abcd=\mathbf{H}} \\ L(1, a)L(1', b)L(c, 2)L(d, 4) \delta_{22'}\delta_{44'}\delta_{13}\delta_{1'3'} \end{aligned} \quad (16)$$

with $N_H = \ell^5/48\pi k^2$ and \mathbf{H} the location of the Hikami vertex in the medium. The diffuse kernel L was defined earlier in Eq. (8). With this, the background energy density at position R is given by,

$$\begin{aligned} B_2(R) = |F|^2 N_H \int_{11'24} \int d^3 \mathbf{H} \sum_{ij}^N \\ |G(2, S)|^2 |G(4, R)|^2 |G(1, \mathbf{x}_i)|^2 |G(1', \mathbf{x}_j)|^2 \\ \times [\nabla_{\mathbf{H}} L(1, \mathbf{H}) \cdot \nabla_{\mathbf{H}} L(1', \mathbf{H}) L(\mathbf{H}, 2) L(\mathbf{H}, 4) \\ + L(1, \mathbf{H}) L(1', \mathbf{H}) \nabla_{\mathbf{H}} L(\mathbf{H}, 2) \cdot \nabla_{\mathbf{H}} L(\mathbf{H}, 4) + \\ + \frac{1}{2} \sum_{i=abcd} -\nabla_i^2 L(1, a) L(1', b) L(c, 2) L(d, 4)]_{abcd=\mathbf{H}} \end{aligned}$$

All phase factors in Eq. (1) cancel so that all N angular channels are correlated. We approximate $|G(2, S)|^2 \approx (\ell/4\pi)\delta_{2,S}$ which may have to be reconsidered for $R \approx S$ in the last line in the expression above that will actually dominate. After some straightforward algebra we find the lengthy expression for the half-space

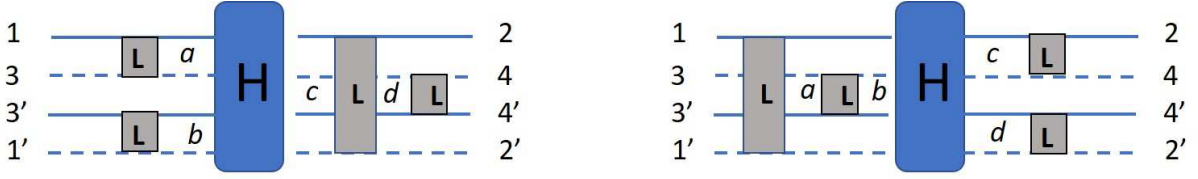


Figure 2. Hikami diagrams for C_2 correlations in the average $\langle T(2, 1)T^*(3, 4)T^*(2', 1')T(3', 4') \rangle$ to focalization. Dashed lines denote complex conjugates. The Hikami vertex H exchanges momenta at position \mathbf{H} in the medium, over which is to be integrated.

$$\begin{aligned}
B_2(R) &= |F|^2 N^2 N_H \frac{\ell^2}{(4\pi)^2} \times \\
&\int_0^\infty dz_1 e^{-z_1/\ell} \int_0^\infty dz_1' e^{-z_1'/\ell} \\
&\times \left[-\frac{1}{2} \partial_{z_H} A(z_H = 0, R, S) \tilde{L}(1, 0) \tilde{L}(1', 0) \right. \\
&+ \frac{1}{2} \partial_{z_H} \left(\tilde{L}(1, z_H = 0) \tilde{L}(1', z_H = 0) \right) A(z_H = 0, R, S) \\
&+ 2 \int_0^\infty dz_H \partial_{z_H} \tilde{L}(1, z_H) \partial_{z_H} \tilde{L}(1', z_H) A(z_H, R, S) \\
&\left. + \int d^3 \mathbf{H} (-\nabla_c^2 - \nabla_d^2) \tilde{L}(1, z_H) \tilde{L}(1', z_H) L(c, S) L(d, R) \right] \quad (17)
\end{aligned}$$

where we have written $\tilde{L}(z, z') = L(z, z', \mathbf{q} = 0)$, defined z_H as the z -component of the location \mathbf{H} of the Hikami box, and introduced, for $R = (z, \boldsymbol{\rho})$

$$\begin{aligned}
A(z_H, R, S) &= \int d^2 \boldsymbol{\rho}_H L(z_H, z_S, \boldsymbol{\rho}_H) L(z_H, z, \boldsymbol{\rho}_H - \boldsymbol{\rho}) \\
&= \int \frac{d^2 \mathbf{q}}{(2\pi)^2} L(z_H, z_S, \mathbf{q}) L(z_H, z, \mathbf{q}) e^{-i\mathbf{q} \cdot \boldsymbol{\rho}}
\end{aligned}$$

which for $z_H \approx 0$ is proportional to the C_1 background in Eq. (11). We will simplify the above expression dramatically. As done before we replace the integrals over the skin layer by $\ell f(0)$ when possible. In the first two terms of Eq. (17) the Hikami vertex is located exactly at the boundary. Their sum is proportional to $A(z_H = 0, R, S) - 2z_0 \partial_{z_H} A(z_H = 0, R, S) \approx 0$ since $A \sim (z_H + z_0)^2$ for $z_H < 0$. In the third term the Hikami box is situated in the skin-layer $0 < z_H < \ell$ since the diffuse propagator in a half-space $\partial_{z_H} \tilde{L}(1, z_H)$ vanishes for $z_H > z_1$. Therefore it is proportional to $A(z_H = 0, R, S)$ and constitutes as such a correction to the C_1 expression derived in Eq. (11),

$$B_2^{(3)}(R) = \frac{9|F|^2 N^2}{(k\ell)^2} \times 3\pi A(0, R, S) = \frac{3\Omega_A}{4\pi} B_1(R) \quad (18)$$

This confirms the angular coverage $\Omega_A/2\pi$ to be the leading parameter in our expansion of wave correlations.

depth z	$B_2(z, 0)/B_1(z, 0)$
$z = 0$	$3\Omega_A/4\pi \times (1 + 2z_0/\ell)$
$z = z_S$	$3\Omega_A/4\pi \times (1 + 4\eta z_S^2/\ell^2)$
$z = \infty$	$3\Omega_A/4\pi \times (1 + 2z_S/\ell)$

Table I. Ratio of C_2 and C_1 contributions to energy density at point $R = (z, \boldsymbol{\rho} = 0)$. The first term “1” in brackets is $B_2^{(3)}$, the second term is $B_2^{(4)}$. Both terms are of same order at $z = 0$, but the second term rapidly dominates as the depth z increases. The ratio B_2/B_1 is a competition of the limited angular coverage of the array $\Omega_A/2\pi \ll 1$ and the large factor z_S/ℓ , especially near the focal point $S = (z_s, \boldsymbol{\rho} = 0)$ ($\eta = 1.38$).

Finally, in the last term the Hikami box is located either *exactly* either at the virtual source S or at the detection point R . The two diffusion operators generate $\delta_{\mathbf{H}, \mathbf{R}} L(\mathbf{H}, \mathbf{S}) + \delta_{\mathbf{H}, \mathbf{S}} L(\mathbf{H}, \mathbf{R})$. This contribution $B_2^{(4)}$ can be interpreted as a diffuse propagation from the slab boundary first to R and subsequently to S , or *vice versa*.

$$\begin{aligned}
B_2^{(4)}(R) &= \frac{9|F|^2 N^2}{(k\ell)^2} \frac{3z_0^2}{2\ell} \times \\
&\left[\frac{1}{\sqrt{(z - z_S)^2 + \rho^2}} - \frac{1}{\sqrt{(z + z_S + 2z_0)^2 + \rho^2}} \right] \quad (19)
\end{aligned}$$

It is singular when $S = R$, but a more detailed analysis (see Appendix B) shows that this is an artifact of a previous approximation near the focal point S and that in reality the singular term smears out over one mean free path and takes the finite value η/ℓ with $\eta = 1.3863$ for $R = S$. Since the C_1 peak is typically one wavelength in size, the C_2 density (19) can still be considered as “background”. Nevertheless, as soon as $R \approx S$ within a wavelength an extra factor 2 shows up because of the existence of “Coherent Backscattering” of waves released by the pointlike source above and due to the so far neglected second term in Eq. (7). However, because the source is smeared out over a mean free path its peak value is suppressed, hence it will not be discussed in further detail.

Let us compare the energy density B_2 produced by C_2 to the density B_1 of the C_1 background found in Eq. (11), and calculate their ratio as a function of the depth z of point R , as is summarized in Table I. The data in the table show that eventually B_2 always dominates, as z_s/ℓ

becomes large enough to compensate for the small factor $3\Omega_A/(4\pi)$. Near the boundary the ratio B_2/B_1 is small and independent of z_S . If the quality of the focusing near S is dominated by B_2 , Eq. (13) must be replaced by the much larger ratio of background to focal peak that is equal to

$$\frac{B_1 + B_2}{P_1(R=S)} \approx \frac{3\eta}{2} \frac{1}{(k\ell)^2} \quad (20)$$

This is sufficiently small for the focusing to be efficient. It is independent of the depth z_s of the focal point and independent of the angular coverage Ω_A as well. Contrary to the B_1 energy density discussed in the previous section, Eq. (19) contains genuine source of energy at the focal point S . The flux emitted by this source is given by $F_S = -D \int d^3\mathbf{r} \nabla^2 B_2^{(4)}(\mathbf{r})$ where the volume integral is to be taken around the point S , see Appendix A. We can compare this to the total flux (15) leaving the sample and find,

$$\frac{F_S}{F_1(z < 0)} = \frac{\Omega_A}{\pi} \quad (21)$$

i.e., the relative source strength created by the wave-front shaped signal in the medium depends (only) on the angular coverage of the array and is determined by Ω_A . The ratio is small because of the large C_1 source created at the incident boundary.

IV. WAVE FRONT FOCUSING TO A POINT IN A SLAB

In the following we show that the above considerations for a half-space change only quantitatively when the focus is performed inside a slab of finite width L . The slab geometry is interesting because it allows to investigate the relation between transmission and focus.

In the C_1 approximation, the background energy density associated with is still given by Eq. (10) but involves the diffuse propagator for a finite slab. Using radiative boundary conditions at both sides $z = -z_0$ and $z = L+z_0$

$$L(z, z', \mathbf{q}) = \frac{12\pi \sinh q[B - \max(z, z') - z_0] \sinh q[\min(z, z') + z_0]}{\ell^3 q \sinh qB} \quad (22)$$

with $B = L + 2z_0$. Equation (10) becomes,

$$B_1(z, \rho) = \frac{9|F|^2 N^2 z_0^2}{(k\ell^2) \Omega_A} \int d^2\mathbf{q} e^{i\mathbf{q}\cdot\rho} \times \frac{\sinh q(B - z_S - z_0) \sinh q(B - z - z_0)}{\sinh^2 qB} \quad (23)$$

valid for $z_S, B \gg z_0$. With the expression for $L(z, z', \mathbf{q})$ for the slab, the peak value in Eq. (9) for a half-space is

modified by

$$P_1(S, R) = 9|F|^2 N^2 P(S, R)^2 \frac{z_0^2}{\ell^2} \left(1 - \frac{z_S + z_0}{B}\right)^2 \quad (24)$$

which in a finite slab decreases smoothly with the depth of S . The ratio of background to peak can be written as,

$$\frac{B_1(R=S)}{P_1(R=S)} = \frac{2\pi/[2k(z_S + z_0)]^2}{\Omega_A} R \left(\frac{z_S + z_0}{B}\right) \quad (25)$$

The function $R(\tau_S)$ rises from the value $R(0) = 1$ for the half-space to $R(1/2) = 2.772$ in the middle of the slab to $R(1) = 7.207$ at the transmitting boundary. The same function R modifies the transverse width of the background energy density $\langle \rho^2 \rangle_1$ around the focus S given by Eq. (12) for a half-space: $\langle \rho^2(z = z_S) \rangle_1 \rightarrow \langle \rho^2 \rangle_1 / R(z_S + z_0/B)$. The finite thickness of the slab thus enhances the background and suppresses the transverse size. Nevertheless, the ratio B_1/P_1 still decays essentially as $1/(kz_S)^2 \Omega_A \ll 1$.

The C_2 background density for the finite slab is given by Eq. (17), though with only an additional first term due to the transmitting boundary $z_H = L$, and which cancels for the same reason due to the radiative boundary condition. If we neglect all powers in ℓ/B we see that the third term $B_2^{(3)}$ only contributes when the Hikami box resides in the skin layer so that the relation $B_2^{(3)}/B_1 = 3\Omega_A/4\pi$ for the half space continues to apply for the slab. The last term of Eq. (17) becomes equal to

$$B_2^{(4)}(z, \rho) = \frac{9|F|^2 N^2 3\pi z_0^2}{(k\ell)^2 \ell} \rho(z, z_S, \rho) \times \left[\left(1 - \frac{z + z_0}{B}\right)^2 + \left(1 - \frac{z_S + z_0}{B}\right)^2 \right] \quad (26)$$

where the $\rho(z, z_S, \rho)$ is the energy density emitted by a diffuse point source at position $z = z_S, \rho = 0$ in the slab, given by

$$\rho(z, z_S, \rho) = \int \frac{d^2\mathbf{q}}{(2\pi)^2} e^{i\mathbf{q}\cdot\rho} \times \frac{\sinh q[B - \max(z, z_S) - z_0] \sinh q[\min(z, z_S) + z_0]}{q \sinh qB}$$

This expression diverges at the focal point S because an energy source is created that is in reality smeared out over a mean free path. The power emitted by this source is slightly lowered for a finite slab and Eq. (21) is modified by,

$$\frac{F_S}{F_1(z < 0)} = \frac{\Omega_A}{\pi} \left(1 - \frac{z_S + z_0}{2B}\right) \quad (27)$$

This ratio slowly decays to $\Omega_A/2\pi$ as the focal point S approaches the transmitting boundary.

The varying background energy density in the slab will have a non-zero transmission coefficient. Because of the

wavefront-shaped incident beam this transmission will not necessarily decay as $1/B$. We shall assume the slab to be optically thick enough so that $\ell/L \ll \Omega_A/\pi \ll 1$. The transmission induced by C_1 is proportional to $(\ell/L)/\Omega_A$, so that C_2 dominates, and in particular the source term $B_2^{(4)}$ given by Eq. (26)

$$\begin{aligned} F_2^{(4)}(L) &= -D \int d^2 \rho \partial_z B_2^{(4)}(z, \rho) \\ &= 9 \frac{|F|^2 N^2}{(k\ell)^2} \pi z_0^2 v_E \left(\frac{z_S + z_0}{B} \right) \left(1 - \frac{z_S}{B} \right)^2 \end{aligned}$$

where we neglected powers of z_0/B . For a finite size of the slab, the reflected current in Eq. (15) achieves an extra factor $(1 - z_S/B)$ due to the presence of $L(0, z_S)$. The normalized transmission is thus equal to

$$T = \frac{\Omega_A}{2\pi} \frac{z_S + z_0}{B} \left(1 - \frac{z_S + z_0}{B} \right) \leq \frac{\Omega_A}{8\pi} \quad (28)$$

By focusing to a point in the slab, the transmission takes a finite value and takes its largest value $T = \Omega_A/8\pi$ independent of thickness B when we focus in the middle of the slab.

On one hand it is surprising to find that WFS to a point facilitates to transmit - via non-Gaussian C_2 correlations - in a non-Ohmic way. On the other hand, the maximum transmission is far from the optimal transmission $T = 1$ established from random matrix theory in quasi-1D samples. This is clearly due to the large C_1 reflection coefficient that stems from the traditional source created near the incident boundary. The modes with optimized transmission somehow find a way to suppress this source. Note also that the energy density expressed by Eq. (26) is not mirror-symmetric, not even when $z_S = B/2$. The density associated with optimized transmission must be mirror-symmetric in the plane $z = B/2$ (see argument below). This is clearly due to our choice to put the time-reversal array on the left, and not on the right, and can be fixed by using identical, independent arrays on both sides.

We conclude that the focalisation to a point in the slab is not equivalent to optimizing transmission. Nevertheless, focusing to a point enhances the transmission far beyond the Ohmic expectation ℓ/L , due to the presence of a source of energy inside the medium.

V. TOWARDS OPTIMIZED TRANSMISSION

In this section we develop the idea that optimizing transmission is related to the creation of an energy source inside the slab. We will show that different propositions for the energy density profile lead to quite different profiles for the sources. Two general arguments are made.

The first argument concerns the spatial symmetry of the density. The procedure is to first optimize the WFS for each different realization to find perfect transmission

and next to average the associated energy density inside the slab over all realizations, and with equal incident power. Having found a wavefront that gives full transmission ($T = 1$) for a given realization of the disorder in the slab, see Figure 3 (Left), the time-reversed operation reproduces the same process, see Figure 3 (Center), gives again an optimal transmission ($T = 1$) with the same density profile. More precisely, this follows from the Stokes relation for the complex transmission matrix for the reversed process, \tilde{t} obeys $\tilde{t}_{nm} = t_{mn}$. If we next perform a mirror operation of both wave and disorder, see Figure 3 (Right), we have constructed an incident wavefront that has the inverted energy density $\tilde{\rho}(x, y, z) = \rho(x, y, L - z)$ with respect to the initial process, with also maximum transmission. Assuming that we perform a perfect average over disorder, both energy densities will occur with same statistical weight. The energy density, averaged over disorder *given* optimal transmission $T = 1$, must be *symmetric* about the central plane of the slab: $\rho_M(z) = \rho_M(L - z)$. Of course, this argument relies on the symmetry of the slab geometry and does no longer apply when the geometry itself breaks mirror symmetry [6].

The second argument, detailed in Appendix A, is that optimization to a point S in the medium produces an energy density whose average obeys a diffusion equation with the usual radiative boundary conditions at both sides, with same diffusion constant, and with some source related to the focal point proportional to the incident power. Optimizing to a focal point is not equivalent to optimizing transmission, but let us speculate that the argument also applies for optimized transmission. This feature is confirmed by numerical simulations [19]. The energy density averaged over different optimizations of transmission $\rho_M(z, \rho)$, must then be a superposition of the complete set of eigenfunctions of the diffusion equation, with a source profile to be determined [4]. Let us ignore the complication of transverse energy profile, and integrate either over ρ or restrict to a quasi-1D geometry. The energy density would then be ($B = L + 2z_0$),

$$\rho_M(z) = \frac{BS}{2\pi D} \sum_{n=1}^{\infty} \rho_M(n) \sin \frac{(2n-1)\pi(z+z_0)}{B} \quad (29)$$

featuring only the *symmetric* modes with odd n , and a front factor that depends on the source power S , including the total amount of energy S delivered by a hypothetical source, and with dimensionless coefficients $\rho_M(n)$ that determine the spatial density profile. For a *single* realization of disorder, no rigorous relation exists between density gradient and transmission and optimization leads to zero reflection $R = 0$ and perfect transmission $T = 1$. After averaging however, the diffusion picture emerges and the gradient of ρ_M at the boundaries determines the average outgoing flux, equal on both sides, hence $R = T$ and $R + T = S$. The source density $S(z)$ is then given

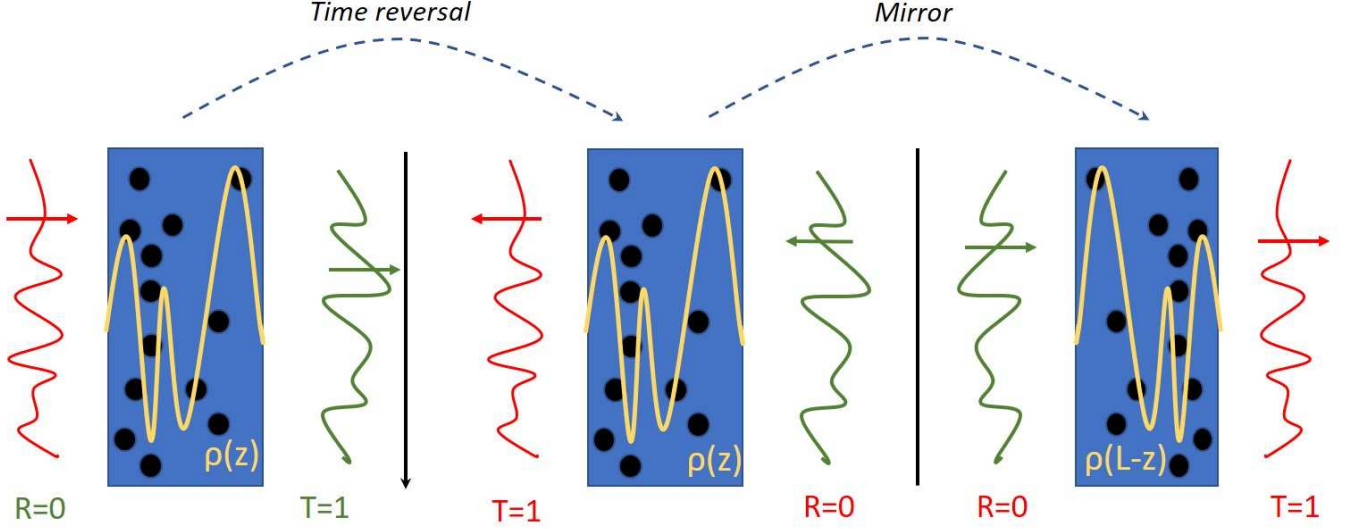


Figure 3. wavefront shaping and the energy density inside a slab. Left: if we optimize the total transmission, it is unity ($T = 1$), whereas total reflection vanishes ($R = 0$) and the energy density $\rho(z)$ varies wildly. Center: if we apply time-reversal, the incident pattern (from left panel) is incident from the back surface without reflection ($R = 0$) and perfectly transmitted ($T = 1$) to the left entrance surface. The energy density $\rho(z)$ has the same pattern as it is not affected by time reversal. Right: if we apply a mirror operation, the incident wavefront from the center image is incident from the left, enters perfectly with ($R = 0$) and transmits perfectly ($T = 1$) to the right. The energy density $\rho(z)$ is mirrored with respect to left and center since the sample structure has been mirrored. Averaging over configurations yields a mirror symmetric energy density, hence $\rho_M(z) = \rho_M(L - z)$.

model	virtual source [S/B]	energy density [BS/D]	$\rho_M(n)$	energy [B ² S/π ² D]	$\rho_M(L/2)/\rho_M(0)$ [B/ℓ]
delta	$\delta(\tilde{z} - 1/2)$	$\frac{1}{4}(1 - 1 - 2\tilde{z})$	$4(-1)^{n-1}/\pi(2n - 1)^2$	1.234	0.750
log-singular	$-\frac{\pi}{4G} \log \tan \frac{\pi}{2} \tilde{z} - \frac{1}{2} $	not ana	$(-1)^{n-1}/G(2n - 1)^3$	1.080	0.548
$n = 1$	$\frac{\pi}{2} \sin \pi \tilde{z}$	$\frac{1}{2\pi} \sin \pi \tilde{z}$	$\delta_{n,1}$	1.000	0.477
best fit	$\frac{1 - \alpha(3\tilde{z}^2 - 3\tilde{z} + 1)}{[1 - \alpha\tilde{z}(1 - \tilde{z})]^3}$	$\frac{1}{2} \frac{\tilde{z}(1 - \tilde{z})}{1 - \alpha\tilde{z}(1 - \tilde{z})}$	0.9966, -0.00295 $+ \mathcal{O}(1)/(2n - 1)^{3.36}$	0.996	0.295
($\alpha = 4 - \pi$) Flat [] ($\alpha = 0$)	1	$\frac{1}{2}\tilde{z}(1 - \tilde{z})$	$8/(\pi^2(2n - 1)^3)$	0.822	0.375
symmetric	$B\delta(z)/2$	$\tilde{z}/2$ ($z < 0$)	$\sin \pi(2n - 1)\tilde{z}_0$	$\pi^2/2$	ℓ/B
normal	+	$\tilde{z}_0/2$ ($0 < z < L$)	×	×	
incidence	$B\delta(L - z)/2$	$(1 - \tilde{z})/2$ ($z > L$)	$4/\pi(2n - 1)^2$	$\tilde{z}_0 - \tilde{z}_0^2$	

Table II. Some properties of 6 different models for a 3D slab integrated over transverse dimensions ρ or alternatively for a quasi-1D geometry. The total energy rate of all sources is normalized to S . We have abbreviated $\tilde{z} \equiv (z + z_0)/B$, $B = L + 2z_0$, $\tilde{z}_0 = 2\ell/3B$, and $G = 0.915965..$ is Catalan’s constant. The “best fit” model was used by Ref. [6] with Fourier coefficients that decay relatively fast and roughly as $1/(2n - 1)^{3.36}$. The symmetric plane wave source corresponds to equal plane waves incident on both sides creating sources near both boundaries.

by

$$S(z) = \frac{\pi S}{2B} \sum_{n=1}^{\infty} \rho_M(n) (2n - 1)^2 \sin \frac{(2n - 1)\pi(z + z_0)}{B} \quad (30)$$

which is thus necessarily also symmetric around $z_S = L/2$. The extra factor $(2n - 1)^2$ implies the resurrection of high-order eigenfunctions in the Fourier expansion for the source that are not all positive-definite. Alternating signs with $\rho_M \sim (-1)^{n+1}$ generate more weight in the

center since for even n the eigenfunctions are all negative at the center of the sample.

In Table II we consider 6 different normalized sources. They all share positive energy density *and* positive source density. The “flat” model was previously discussed by Davy *et al.* and corresponds to a homogeneous source density [5]. This model was generalized by Koirala *et al.* to the “best fit” model and the best fit to numerical simulation was obtained for $\alpha \approx 4 - \pi$ [6]. Furthermore, the simplest model “ $n = 1$ ” keeps only the first eigen-

function, the only symmetric one that is positive definite. Finally, the “symmetric normal incidence model” is associated with two equal sources close to both boundaries. This model clearly behaves differently from the others, because it decays slower with n and the Fourier coefficients explicitly depend on ℓ/B .

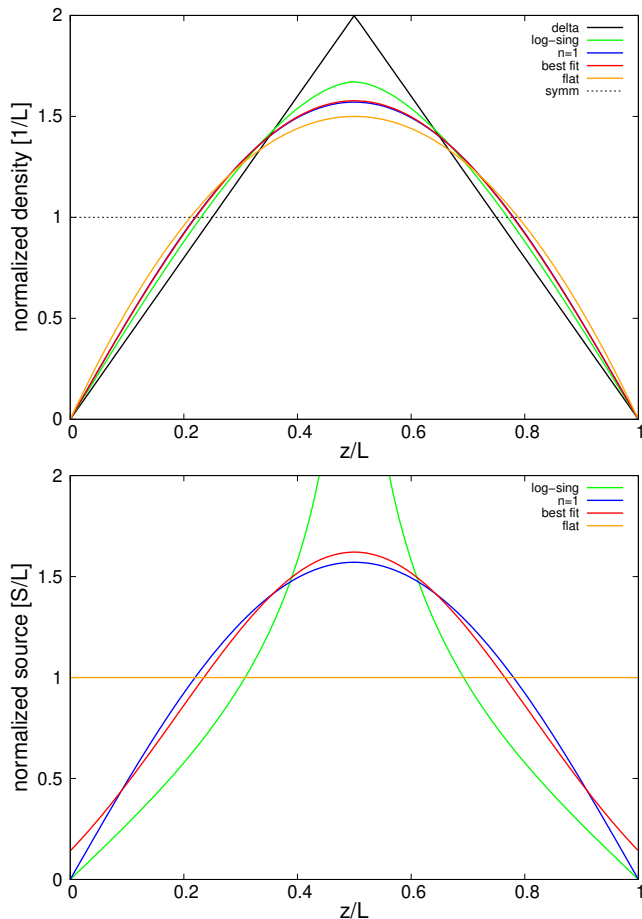


Figure 4. Normalized energy densities (top) and normalized sources (bottom) for the six different models that are specified in Table II.

The assumption of a positive-definite, mirror-symmetric source density filters out many solutions but clearly does not fix the profile. The total source power is normalized to S by imposing $\sum_{n=1}^{\infty} \rho_M(n)(2n-1) = 1$ so that $\rho_M(n)$ must decay at least as fast as $1/(2n-1)^3$. This would explain partly that different models for the density profile in Table II have very similar shapes, especially when they are each normalized, see Figure 4. An extreme case, referred to as “delta” having a point source in the middle of the slab can be clearly disqualified by numerical simulations that favor the “best fit model”. In Figure 4 we see that the source distributions vary strongly from one model to the other. The models “ $n=1$ ” and “best fit” have rather similar sources but hardly distinguishable energy densities.

This discussion suggests that in order to discriminate between different models for optimized transmission, one

should focus on the source density profile, rather than on the energy density. The “ $n=1$ ” model seems to be an accurate candidate, but numerical simulations do reveal the existence of higher modes, 2% of the energy according to [4]. The “best-fit model” has a finite source density near the boundaries, which is physically reasonable. It is also remarkable that the very small value for $\rho_M(n=2)$ is $10\times$ smaller than the one for the flat model. Finally we can investigate the total energy in the slab associated with optimized transmission. Total energy for optimized transmission can be related to average dwell time for the waves emitted by the source to reach the boundary [15]. For $R=0$, $T=S=1$,

$$\int d^3\mathbf{r} \rho_M(\mathbf{r}) = \frac{d\phi_T}{d\omega}(\rho) = \frac{B^2}{\pi^2 D} \sum_{n=1}^{\infty} \frac{\rho_M(n)}{2n-1} \quad (31)$$

The dwell time itself can be optimized [16] or manipulated [9] as well as the closely related delay time [3]. We infer from Table II that the stored energy varies only weakly among the different models for optimized transmission. This is due to the fact that the Fourier components in Eq. (31) decay as fast as $1/(2n-1)^4$. Because phase is measurable after optimizing transmission, this could be an opportunity to measure the diffusion coefficient in optimized transmission.

VI. CONCLUSION

In this work we have applied mesoscopic speckle theory to describe the energy density created by a wavefront-shaped incident signal that focuses on a point in the random medium. The focus is determined by the short-range C_1 -speckle whereas the long-range C_2 speckle creates a background energy density that dominates deep inside the medium. This part also generates an energy source inside the medium. The focus is due to constructive interference between incoming and outgoing spherical waves, like in time-reversal experiments, and not to the source. Because C_1 speckle creates a source near the incident boundary, much like an incident plane wave usually does in radiative transfer, the focusing to a point does not optimize transmission. We have developed the idea that optimizing transmission removes this C_1 source and creates a mesoscopic energy source inside the sample that is mirror-symmetric. Different models for this source produce quite similar profiles for the energy density, close to the first eigenmode of the diffusion equation as observed in numerical simulations. The red curve labeled “best fit” in Figure 4b represents undoubtedly the energy source that optimizes transmission and is close yet not equal to the lowest diffusion mode. A major challenge exists to understand this profile from first principles.

ACKNOWLEDGMENTS

We thank Sergey Skipetrov for useful discussions. WLV thanks the CNRS for a fellowship as guest investigator. WLV and AL acknowledge support by NWO-TTW Perspectief program P15-36 “Free-form scattering optics” (FFSO) in collaboration with TU Delft, TU Eindhoven, and industrial users ASML, Demcon, Lumileds, Schott, Signify, and TNO, as well by NWO-TTW Perspectief program P21-20.

VII. APPENDIX

Appendix A: Current of wave-front shaped waves

1. Current of the background signal

The expressions for the background densities in both the C_1 and C_2 approximation can be generalized to the spatial correlation function

$$\langle \Phi(\mathbf{r})\Phi(\mathbf{r}')^* \rangle = \int d^3\mathbf{r}_4 f(\mathbf{r}_4)G(4, \mathbf{r})G^*(4, \mathbf{r}') \quad (\text{A1})$$

with G the bulk Dyson Green’s function given in Eq. (2) and $f(\mathbf{r})$ some real-valued function obtained from correlation functions that varies slowly on the scale of the mean free path. For monochromatic scalar waves the cycled-averaged (radiative) density is proportional to $\rho(\mathbf{r}) = |\Phi(\mathbf{r})|^2$. For $\mathbf{r} = \mathbf{r}'$ we neglect spatial variation of $f(\mathbf{r})$ within a mean free path and use Eq. (6) giving

$$\rho(\mathbf{r}) = \frac{\ell}{4\pi} f(\mathbf{r}) \quad (\text{A2})$$

The cycle-averaged current-density is $\mathbf{J} = (c_0^2/\omega)\text{Im}\Phi^*(\mathbf{r})\nabla\Phi(\mathbf{r})$. Using $\text{Im}G^*(\mathbf{r})\nabla G(\mathbf{r}) = k\hat{\mathbf{r}}|G(\mathbf{r})|^2$, we find from Eq. (A1), putting $\mathbf{x} = \mathbf{r} - \mathbf{r}_4$

$$\begin{aligned} \mathbf{J}(\mathbf{r}) &= \frac{kc_0^2}{\omega} \int d^3\mathbf{x} f(\mathbf{r} - \mathbf{x})\hat{\mathbf{x}}|G(\mathbf{x})|^2 \\ &\approx \frac{kc_0^2}{\omega} \int d^3\mathbf{x} (-\nabla f(\mathbf{r}))\mathbf{x}\hat{\mathbf{x}}|G(\mathbf{x})|^2 \\ &= -\frac{1}{3} \frac{c_0^2}{v_P} \ell \times \nabla\rho(\mathbf{r}) \end{aligned} \quad (\text{A3})$$

with v_P the phase velocity. This implies that the diffusion equation applies despite no matter where $f(\mathbf{r})$ stems from, here from two-particle diagrams, and with the same diffusion coefficient as the one found for the one-particle Green’s function (the matter energy density inside scatterers should be treated to find the correct velocity). Any source or sink of energy in the medium is characterized by a non-zero value for $\nabla^2\rho(\mathbf{r})$.

2. Current of focused signal

The average field at a point \mathbf{r} near the focal point S follows from Eq. (3),

$$\Phi(\mathbf{r}) = NF \int_1 \int_2 e^{-z_1/\ell} L(1, 2)G(S, 2)G^*(2, \mathbf{r}) \quad (\text{A4})$$

Recall that the factor F has the same unit as the field unit, and that $|F|^2$ has the dimension of field energy density. This expression contains a rapidly varying part on the scale of the wavelength, as well as an exponential decay of the Green’s function $G(x)$ on the scale of the mean free path. Because L varies slower on this scale we can substitute $\mathbf{x} = \mathbf{r} - \mathbf{r}_2$ and $\mathbf{y} = \mathbf{r} - \mathbf{r}_S$, and expand $L(1, 2)$ around \mathbf{r} as,

$$\int_2 \rightarrow \int d^3\mathbf{x} G(\mathbf{x} - \mathbf{y})G^*(\mathbf{x}) [L(1, \mathbf{r}) - \mathbf{x} \cdot \nabla_{\mathbf{r}} L(1, \mathbf{r})]$$

The integral over \mathbf{r}_1 generates $\ell L(0, z, \mathbf{q} = 0) \equiv \ell\tilde{L}(0, z)$. The integral over \mathbf{x} can be performed to find,

$$\Phi(z) \sim NF\ell^2 \left[P(y)\tilde{L}(0, z) + i\frac{\ell}{k} P'(y)\nabla_{\mathbf{r}}\tilde{L}(1, z) \cdot \hat{\mathbf{y}} \right] \quad (\text{A5})$$

with $P(y) = -\text{Im}G(y)$. The second term in the expansion is usually identified with current but here represents a bipolar contribution to the angular dependence of the focused field around the point S . The current density associated with the focused signal is given by $\mathbf{J} = (c_0/k)\text{Im}\Phi^*\nabla_{\mathbf{r}}\Phi$, involving the *average* field Φ . The released energy at distance y from the focal point follows from the energy flow through a surface $A = 4\pi y^2$ around the source,

$$F(y) = \int d^2\mathbf{A} \cdot \mathbf{J}(S, \mathbf{y}) \quad (\text{A6})$$

The derivatives $\nabla_{\mathbf{y}}(\mathbf{y}P)$ cancel by parity in the angular integral. The derivative ∂_z survives and we obtain,

$$F(y) = -\frac{N^2|F|^2 c_0 \ell^5}{3k^4} y^2 P(y)P'(y) [\nabla_{\mathbf{r}} L(1, \mathbf{r} = S)]^2 \quad (\text{A7})$$

and decays exponentially with the mean free path. Therefore, the focused signal is not associated with a net source and $S = \int d^3\mathbf{r} s(\mathbf{r}) = 0$.

Appendix B: peak value for diffuse C_2 source

The Hikami source derived in Eq. (17) is proportional to

$$I(\mathbf{r}, \mathbf{r}_S) = \int d^3\mathbf{r}_2 \int d^3\mathbf{r}_4 |G(\mathbf{r} - \mathbf{r}_2)|^2 \frac{1}{|\mathbf{r}_2 - \mathbf{r}_4|} |G(\mathbf{r}_S - \mathbf{r}_4)|^2$$

with $|G(\mathbf{x})|^2 = \exp(-x/\ell)/(4\pi x)^2$. For \mathbf{r}_S and \mathbf{r} separated by more than a mean free path ($|\mathbf{r}_S - \mathbf{r}| > \ell$) the two integrals decouple, and using Eq. (6), the Hikami source takes the form of a point source:

$$I(\mathbf{r}, \mathbf{r}_S) = \left(\frac{\ell}{4\pi}\right)^2 \frac{1}{|\mathbf{r}_S - \mathbf{r}|} \quad (\text{B1})$$

When \mathbf{r}_S and \mathbf{r} are closer this is no longer valid. In the limit that both positions coincide ($\mathbf{r}_S = \mathbf{r}$) we get

$$\begin{aligned} I(\mathbf{r}_S, \mathbf{r}_S) &= \frac{\ell}{(4\pi)^4} \int d^3\mathbf{x} \int d^3\mathbf{y} \frac{e^{-(x+y)}}{x^2 y^2} \frac{1}{|\mathbf{x} - \mathbf{y}|} \\ &= \frac{\ell}{(4\pi)^2} 2 \int_0^{\pi/4} \frac{d\phi}{\cos \phi (\cos \phi + \sin \phi)} \\ &= \left(\frac{\ell}{4\pi}\right)^2 \frac{1.3863}{\ell} \end{aligned}$$

This outcome comes down to replacing $1/r$ in Eq. (B1) for $r = 0$ by η/ℓ , with $\eta = 1.3863$.

The power density of the source is equal to $\nabla \cdot \mathbf{J}$. The total power is proportional to

$$\int d^3\mathbf{r} (-\nabla^2) I(\mathbf{r}, \mathbf{r}_S) = 4\pi \left(\frac{\ell}{4\pi}\right)^2 \quad (\text{B2})$$

This means that the point source in Eq. (B1) is in reality smeared out over one mean free path ℓ when \mathbf{r}_S and \mathbf{r} are close, without affecting its total power.

Appendix C: C_0 correlations

The C_0 correlation was first introduced by Shapiro as a fluctuation of the source power by a nearby scatterer, and yields spatial correlations in intensity of infinite range [20]. It was later shown that C_0 correlations are fluctuations of the local density of states (LDOS), to which any source is sensitive [17, 18]. We here consider the importance of C_0 speckle for the quality of the focusing. We emphasize that even if the source S is virtual, the focusing at S is affected by nearby scatterers. The detection point R is assumed to contain no real detector but fluctuations in LDOS at R do exist.

The two C_0 diagrams contributing to this speckle are shown in Figure 5. They describe the perturbation of both background and peak by a scatterer close to R and S . This implies immediately that both diagrams survive

only when R and S are separated by at most one mean free path. Both diagrams thus contribute to the focusing and not to the background, and the infinite correlation of C_0 does not pertain to R . Let us first consider the right-hand side figure. It correlates all incident channels as was the case for the C_1 peak in Eq. [9]. The calculation goes as before leading to Eq.(9) with a minor modification of Eq.(6) that integrates out the positions 2 and 2' near S . For scatterers "p" and scattering matrix t this equation is replaced by,

$$\begin{aligned} \left(\frac{\ell}{4\pi}\right)^2 P(S, R)^2 &\rightarrow 2 \times \int_{2,2'} \sum_p G(2, p) t G(p, S) G^*(2, R) \\ &\quad \times G(2', R) G^*(2', p) t^* G^*(p, S) \\ &= \left(\frac{\ell}{4\pi}\right)^2 \times \frac{8\pi}{\ell} \int d^3\mathbf{r}_p P(p, R)^2 |G(p, S)|^2 \quad (\text{C1}) \end{aligned}$$

where we have replaced $\sum_p = \rho \int d^3\mathbf{r}_p$ and used $\rho |t|^2 = 4\pi/\ell$. The first factor in this equation is just the one found for the C_1 focusing peak, the second factor stands for the relative C_0 correction. The integral over \mathbf{r}_p averages out the oscillation of the sinc-function $P(p, R)$ and this factor decays as $\exp(-|R - S|/\ell)/k^2 |R - S|^2$. For $R = S$ we find the C_0 factor equal to $\pi/k\ell$ consistent with previous work [17].

The diagram on the left of Figure 5 can be dealt with similarly, but suffers from decorrelation between the N channels, like the C_1 background in Eq. (10). This time the nearby scatterers p impose a factor different from the one in Eq. (C1), namely

$$\text{Re} \frac{8\pi}{\ell} \int d^3\mathbf{r}_p P(p, R) G^*(p, R) P(p, S) G(p, S) \quad (\text{C2})$$

A precise analysis shows that this expression decays exponentially with the distance between R and S as well and thus contributes to the peak. For $S = R$ it takes again the value $\pi/k\ell$. However, this C_0 diagram is an extra factor $1/\Omega_A(kz_s)^2$ smaller than the one expressed by Eq. (C1) because this time the N channels are not all correlated. It can thus be neglected.

We conclude that the C_0 correlation contributes to the focusing peak around the virtual source S , with a relative weight $\pi/k\ell$, but does not significantly change the picture put forward by the C_1 approximation. Whereas the latter typically predicts a diffraction-limited function $(\sin kx/kx)^2$, the C_0 peak decays as $\exp(-x/\ell)/(kx)^2$ around S with an amplitude that is a factor $\pi/k\ell$ smaller.

[1] I. M. Vellekoop and A. P. Mosk, "Focusing coherent light through opaque strongly scattering media", Opt. Lett. Vol. **32**(16), 2309-2311 (2007).
[2] Mosk, A. P., Lagendijk, A., Lerosey, G. and Fink, M. Controlling waves in space and time for imaging and focusing in complex media. Nat. Photon. **6**, 283-292 (2012).

[3] S. Rotter and S. Gigan, S. Light fields in complex media: mesoscopic scattering meets wave control. Rev. Mod. Phys. **89**, 015005 (2017).
[4] O.S. Ojambati, A.P. Mosk, I.M. Vellekoop, A. Lagendijk and W.L. Vos, Optics Express **24**, (2016).
[5] Davy M, Shi Z, Park J, Tian C, Genack AZ. Univer-

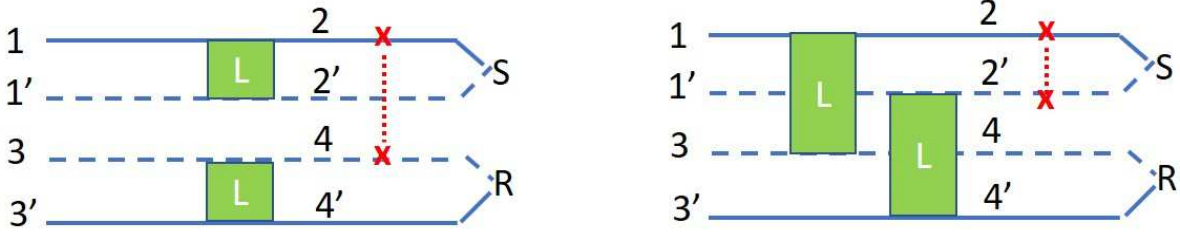


Figure 5. C_0 contributions to the energy density at position R caused by a scatterer (in red) close to the focus locus S . Dashed lines denote complex conjugate wave fields. Both actually generate a contribution to the peak, but only the left diagram suffers from decorrelation between the N channels. Complex conjugates of these diagrams exist but are not shown.

- sal structure of transmission eigenchannels inside opaque media. *Nat Commun.* **20(6)**, 6893 (2015).
- [6] M. Koirala, R. Sarma, H. Cao, and A. Yamilov, *Phys. Rev. B* **96**, 054209 (2017).
- [7] B.A. van Tiggelen, *Phys. Rev. Lett.* **91**, 243904 (2003).
- [8] C.W. Hsu, S.F. Liew, A.L. Goetschy, H. Cao, and D. Stone, *Nature Physics* **13**, 497 (2017).
- [9] Sarma, R., Yamilov, A. G., Petrenko, S., Bromberg, Y. and H. Cao, H. Control of energy density inside a disordered medium by coupling to open or closed channels. *Phys. Rev. Lett.* **117**, 86803 (2016).
- [10] A. Derode, Ph. Roux and M. Fink, *Phys. Rev. Lett.* **75**, 4206 (1995).
- [11] P. Blomgren, G.C. Papanicolaou and H. Zhao, *J. Acoust. Soc. Am.* **111**, 230 (2002).
- [12] M.C.W. van Rossum and Th. M. Nieuwenhuizen, *Rev. Mod. Physics*, **71(1)**, 313 -371 (1999).
- [13] C. Draeger and M. Fink, "One-channel time-reversal in chaotic cavities: Theoretical limits," *J. Acoust. Soc. Am.* **105**, 611–617 (1999).
- [14] W. K. Hildebrand, A. Strybulevych, S.E. Skipetrov, B.A. van Tiggelen, J.H. Page *Physical Review Letters* **112**, 073902 (2014)
- [15] B. A. van Tiggelen, S. E. Skipetrov, J. H. Page, *European Physical Journal - Special Topics* **226(7)**, 1457-1475 (2017).
- [16] M Durand, SM Popoff, R Carminati, A Goetschy, *Phys. Rev. Lett.* **123**, 243901 (2019).
- [17] B.A. van Tiggelen and S. E. Skipetrov *Phys. Rev. E* **73**, 045601 (2006).
- [18] M. D. Birowosuto, S. E. Skipetrov, W. L. Vos, and A. P. Mosk, "Observation of Spatial Fluctuations of the Local Density of States in Random Photonic Media", *Phys. Rev. Lett.* **105**, 013904 (2010).
- [19] Shi, Z., Genack, A.Z. "Diffusion in translucent media," *Nat. Commun.* **9**, 1862 (2018).
- [20] B. Shapiro, "New Type of Intensity Correlation in Random Media", *Phys. Rev. Lett.* **83**, 4733 (1999).